Exploring Single-Photon Recoil on Free Electrons

Alexander Preimesberger,[1,2] Dominik Hornof,[1,2] Theo Dorfner,[1,2] Thomas Schachinger,[2] Martin Hrtoň,[3,4]
Andrea Konečná,[3,4] and Philipp Haslinger[1,2,*]
[1] *Vienna Center for Quantum Science and Technology, Atominstitut, TU Wien, Vienna, Austria*
[2] *University Service Centre for Transmission Electron Microscopy, TU Wien, Vienna, Austria*
[3] *Institute of Physical Engineering, Brno University of Technology, 616 69 Brno, Czech Republic*
[4] *Central European Institute of Technology, Brno University of Technology, 612 00 Brno, Czech Republic*

(Received 25 September 2024; accepted 7 February 2025; published 4 March 2025)

Recent advancements in time-resolved electron and photon detection enable novel correlative measurements of electrons and their associated cathodoluminescence (CL) photons within a transmission electron microscope. These studies are pivotal for understanding the underlying physics in coherent CL processes. We present experimental investigations of energy-momentum conservation on the single particle level, achieved through coincidence detection of electron-photon pairs. This not only enables unprecedented clarity in detecting weak signals otherwise obscured by nonradiative processes but also provides a new experimental pathway to investigate momentum-position correlations to explore entanglement within electron-photon pairs.

DOI: 10.1103/PhysRevLett.134.096901

Transmission electron microscopes (TEMs) are exceptional tools for investigating samples down to single-atom resolution [1,2]. Standard TEM imaging relies on detecting energetic (30–300 keV) electrons of the primary beam transmitted through a thin sample, where most of the electrons interact with the sample elastically. However, a small portion of the inelastically scattered primary electrons can trigger a direct emission of a photon, which is often denoted as "coherent" cathodoluminescence (CL) [3–7]. Such photons can propagate within the sample material (e.g., the so-called Cherenkov radiation [8–10]) or radiate into the vacuum surrounding the sample. In the latter case, we distinguish various processes, such as transition radiation [11–14] and the Smith-Purcell effect [15,16]. Importantly, photons generated during the aforementioned processes carry energy and momentum related to the electron energy loss and momentum recoil of the fast electron [17].

Sophisticated experimental setups have been built to investigate visible photons in the TEM. The photons can be analyzed spectrally, but also based on their polarization and emission angle [18–20]. By employing Hanbury Brown-Twiss interferometry [10,21,22], it is possible to extract photon statistics and reveal properties of CL light. The advent of time-resolved direct electron detectors has enabled simultaneous single-photon and single-electron detection sensitivity and fast (∼ns) signal readout, allowing us to time tag individual electrons and thus identify coincident, correlated electron-photon pairs. Previous works have exploited correlations within the electron-photon pairs to improve the signal-to-noise ratio in X-ray spectroscopy inside an electron microscope [23–25], increase the signal in excitation lifetime analysis [26], map photonic modes [27] and resolve the energy dependence of competing excitation pathways [28] on the single electron-photon level.

In this Letter, we use coincidence detection of electrons and photons to investigate energy-momentum conservation within electron-photon pairs emerging in the "coherent" CL process. By imaging the electron recoil in coincident electron-photon pairs, we obtain a distribution that reflects the momentum distribution of the detected photons. We show that this result can be understood as a direct consequence of momentum conservation between the two particles. Understanding this fundamental property is of crucial importance for the investigation of electron-photon pairs that share a common state in momentum-position space, going beyond classical correlations to explore entanglement [29–32].

Fig. 1(a) gives a general overview of the experimental setup. In a TEM (FEI/TFS Tecnai G2 F20) a continuous beam of electrons with a primary beam energy of $E_{\mathrm{kin}} = 200\ \mathrm{keV} \pm 0.45\ \mathrm{eV}$ (FWHM) and a current of ∼3 pA irradiates the sample. Each electron has a certain probability of coherently producing a CL photon at the interaction time $t = 0$. Independently, the electron can excite the

---

[*] Contact author: philipp.haslinger@tuwien.ac.at

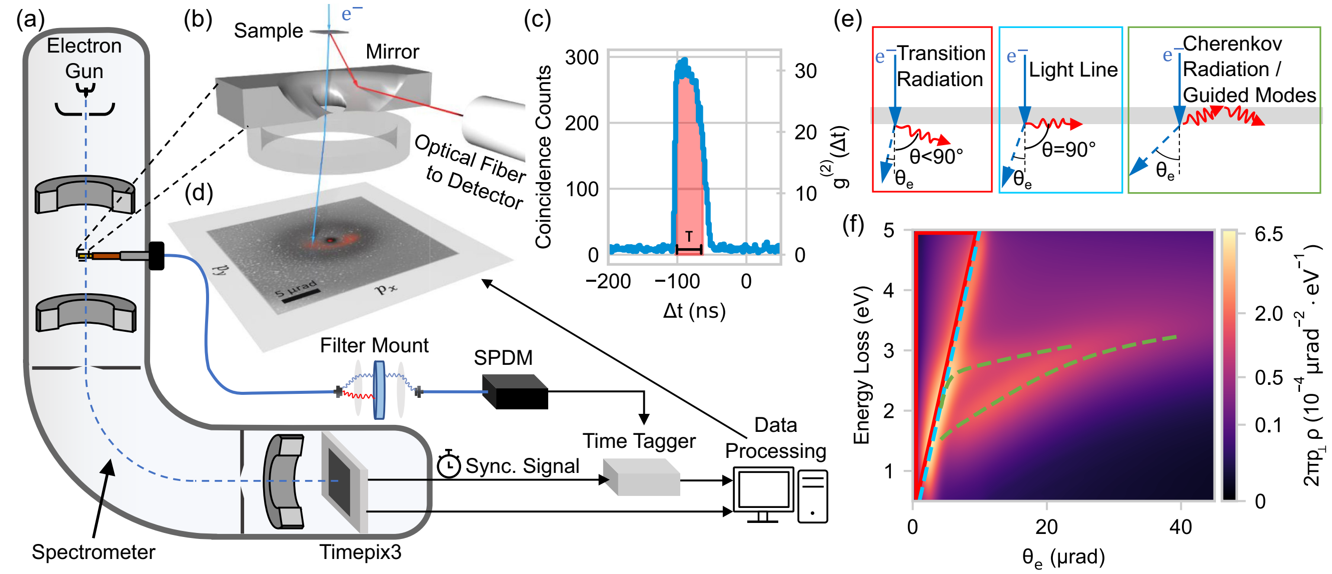

FIG. 1. Experimental setup for detecting coincident electron-photon pairs. (a) A schematic of a TEM with an electron energy filter (spectrometer), where 200 keV electrons interact with a sample (thin silicon membrane). The electrons are detected in diffraction mode with a TP3-based camera and time-stamped. The corresponding CL photons are collected by a Gatan Vulcan sample holder (b) and guided through a multimode fiber to a single photon detection module (SPDM). A time tagger ensures the necessary synchronisation, which enables us to correlate individual photons to their originating electrons in time, clearly visible in a $g^{(2)}$ plot (c) at a certain time delay. These electron-photon pairs can now be analysed collectively, e.g. in terms of energy and momentum (d). The schematics in (e) represent the various CL production mechanisms that contribute to the signal according to their characteristic dispersion relations and photon emission process (see the main text). (f) Displays the calculated probability density of specific energy losses corresponding to angular deflections θ_e of electrons. The overlaid dashed lines trace the most probable paths for the scenarios illustrated in (e) (light line in cyan, guided modes in green). The area framed in red identifies the possible values of momentum transfer due to transition radiation.

sample to incoherently emit a photon after a random delay, depending on the characteristic lifetime of the process [33]. The Gatan Vulcan CL TEM holder features two ellipsoidal mirrors, one above and one below the sample, the bottom mirror is schematically depicted in Fig. 1(b). These mirrors are aligned to collect photons from a focal point at the sample plane and reflect them onto the faces of two separate multimode fibers, which guide the photons to a single-photon detection module (SPDM). Optionally, an optical filter can be applied to investigate only photons in a certain energy range. Each photon detection event is time stamped by the time tagging device, resulting in a recorded value t_γ. The electrons transmitted through the sample further propagate through the microscope. Its magnetic lenses are set to detect the electrons in the diffraction plane, as shown in Figs. 1(b) and 1(d). This configuration is known as diffraction mode. Optionally, the electrons can be energy-filtered using a spectrometer (Gatan GIF Tridiem, post-column imaging filter). Finally, they are directed to a TimePix3 (TP3) direct electron detection camera, which can detect the time of impact of individual electrons, resulting in a time stamp t_e for each of them. The arrival times t_γ and t_e can be correlated in post-processing, resulting in a temporal cross-correlation histogram, an example is shown in Fig. 1(c) [34]. For various reasons (e.g., TP3 detector jitter and/or synchronisation between electron and photon detection) our temporal resolution is limited to about 50 ns. To match electrons with coincident photons, we determine the difference in detection time $\Delta t_{\mathrm{e}\gamma} = t_\mathrm{e} - t_\gamma$ between each photon (t_γ) and the electron (t_e) that matches the expected time delay most closely. A pair of detection events is classified as a coincidence event if the time difference is within $\pm\tau/2 = \pm 25$ ns to the expected value $\mathbb{E}[\Delta t_{\mathrm{e}\gamma}] \approx -80$ ns, i.e. it must fall into the interval $[\mathbb{E}[t_{\mathrm{e}\gamma}] - 25\ \text{ns} < \Delta t_{\mathrm{e}\gamma} < \mathbb{E}[t_{\mathrm{e}\gamma}] + 25\ \text{ns}]$ [34].

We let the electrons interact with a 100 nm thick monocrystalline silicon membrane ($500 \times 500\ \mu\text{m}^2$, in (100)-orientation, Silson Ltd.). Similar samples were shown to support a variety of electron-triggered photon production mechanisms, which were observed using both CL [39–42] and momentum-resolved electron energy-loss spectroscopy (q-EELS) [9,43–45]. We configure the electron microscope to illuminate the Si membrane with a nearly parallel electron beam (diameter ~50 μm at the sample plane) to produce a low-angle diffraction (LAD) image of the zero-order Bragg peak. If the diffraction image is energy-filtered, it clearly exhibits a non-trivial pattern related to the distribution of electron momenta due to the excitation of photons, as demonstrated in the ring-like pattern shown in Fig. 1(d).

To interpret the experimental results, we first calculate the probability density $\rho(E, \mathbf{p}_\perp)$ for an electron that undergoes an energy loss E while acquiring the transverse

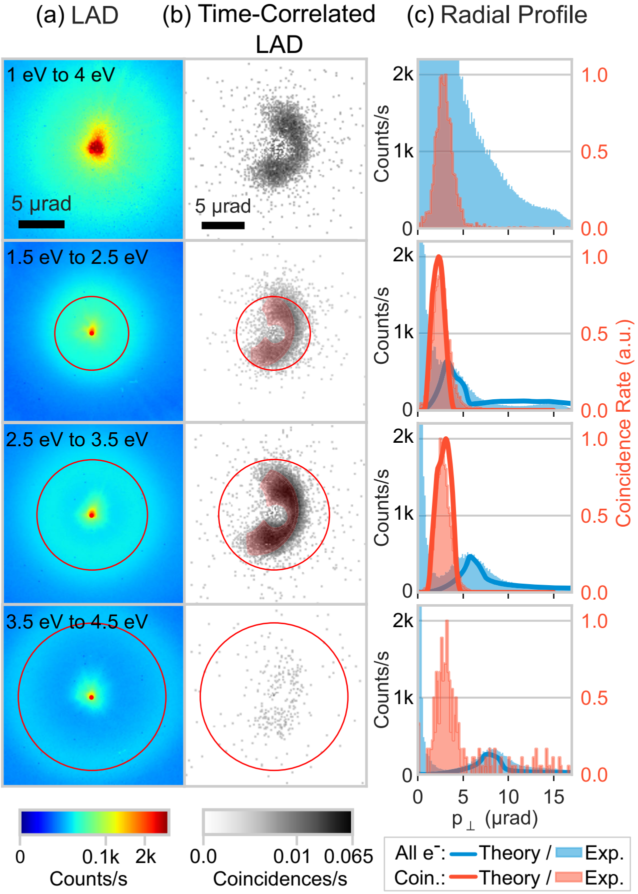

FIG. 2. Energy-filtered low-angle diffraction images are shown without (a) and with (b) coincidence filtering applied. While the light line, as theoretically expected at the red ring, is the most prominent feature in the unfiltered distribution, additional structure corresponding to electron-photon pairs with energy-momentum inside the light line is revealed by applying coincidence filtering. In (c) the integrated radial profiles around the marked center are compared to the theoretical predictions.

momentum $\mathbf{p}_\perp = (p_x, p_y)$. This can be used to infer the electron deflection angle $\theta_\mathrm{e} \approx p_\perp / p_z$, where p_z is the momentum along the electron-beam axis. This calculation, shown in Fig. 1(f), considers the coherent and weak electron-sample interaction. The model [34] embeds the scattering geometry (i.e., electrons moving along a straight trajectory and passing through the 100 nm thin film) and optical properties of silicon characterised by the dielectric function [46]. The energy and transverse momentum in the modeled coherent electron-photon scattering process are conserved: $E = \hbar\omega$, where $\hbar\omega$ is the photon energy, and $\mathbf{p}_{\perp,\mathrm{f}} - \mathbf{p}_{\perp,\mathrm{i}} = -\hbar\mathbf{k}_\perp$, with $\mathbf{p}_{\perp,\mathrm{f/i}}$ being the final/initial electron transverse momentum and $\mathbf{k}_\perp$ being the transverse component of the photon wave vector. Importantly, due to the energy-(transverse) momentum conservation, ρ can be directly mapped on the distribution of the photons emerging in the electron-sample interaction.

The energy-momentum conservation also allows us to assign two distinct scenarios to separate regions of the probability density ρ. Cherenkov emission [9,43–45,47] produces photons propagating inside the Si membrane and causes transverse momentum transfer to the electron below the "light line", which is defined by $p_\perp = \hbar k_0$, with $k_0 = \omega/c$ and the speed of light in vacuum c, see Fig. 1(e) and the corresponding dashed cyan line in Fig. 1(f). In our sample, as a result of the large refractive index $n \approx 4$, Cherenkov photons couple exclusively to guided modes, which do not contribute to the radiative CL signal [39,44,47,48]. On the other hand, the transition radiation consists of photons propagating outside the thin film, emitted at an angle θ with respect to the beam axis. Excitation of transition radiation requires a transverse momentum transfer $p_\perp = \sin\theta \hbar k_0$ from the electron to the photon. Consequently, transition radiation photons are always associated with electrons detected to the left of the light line, i.e., with transverse momentum $p_\perp < \hbar k_0$.

Before presenting our coincidence data, we need to understand the setup that constrains both electron and photon detection. As mentioned previously, we can employ a spectrometer to energy-filter the transmitted electrons. The resulting measured momentum-dependent probability density is then expressed as $\rho(E, \mathbf{p}_\perp)\alpha(E)$, where $\alpha(E)$ is a function that reflects the transmission and rejection of electrons depending on their energy loss. Detection of the far-field photons is slightly more complicated. Our CL setup utilizes ellipsoidal mirrors to collect and fiber-couple CL photons. The mirrors accept photons only from a certain solid angle, as visualized by the 3D plot of the mirror geometry in Fig. 1(b) [34]. We express this geometry limitation of photon collection as well as the efficiency differences in guiding and detecting photons of various momenta and energies with a function $\alpha_\gamma(\hbar\omega, \hat{\mathbf{k}}_\perp)$, where $\hat{\mathbf{k}}_\perp = (k_x/k_0, k_y/k_0)$.

We first analyze the experimental data as a conventional LAD image, without coincidence filtering, and impose energy filtering on the electron side (see Ref. [34] for experimental details). Figure 2(a) shows data that is only minimally filtered (left), compared to narrowly energy-filtered LAD images. The energy filtering is performed within intervals with a width of $2\delta = 1$ eV, each having a different central value E_c, which imposes $\alpha = \mathrm{rect}[(E - E_\mathrm{c})/(2\delta)]$. The intense spot in the middle of the images represents the portion of the undeflected parallel probing beam that passes the energy filter due to the tail of the initial energy distribution of the electron source. The remaining part of the energy-filtered LAD images can be interpreted as $I(\mathbf{p}_\perp) \propto \int dE\, \rho(E, \mathbf{p}_\perp)\alpha(E)$, describing the aggregate distribution for all electrons with an energy-loss value within the accepted range. We observe a dominant ring-like feature, which we attribute to the excitation of CL photons, propagating nearly parallel to the slab's surface. The perimeters of the rings (denoted by red circles) are always located at the light line, i.e., $p_\perp \approx E_\mathrm{c}/c$, which confirms the theoretical prediction of maxima in the energy-momentum dependence of the loss probability in Fig. 1(f). Since these data show rotational symmetry around the center determined by the undeflected part of the beam, we utilize integration over the azimuthal angle ϕ_e to obtain the radial profile as $I(p_\perp) = p_\perp \int d\phi_\mathrm{e} I(\mathbf{p}_\perp)$, where $\phi_\mathrm{e} = \arctan(p_y/p_x)$. The integration increases the signal-to-noise ratio (SNR) and facilitates comparison with the theory [see Fig. 2(c) and blue histograms/lines therein]. When accounting for the imperfect removal of the zero-loss beam, the data (blue shaded area) is in excellent agreement with the theory (solid blue line), considering contributions from all the coherent interaction mechanisms discussed above. This is what we can learn from energy-filtered electron images: we see a distribution of energy loss and deflection that results from a variety of superimposed loss mechanisms with no direct way of identifying which process contributes to the radiative CL signal.

In the following step, we match electrons to photons based on their arrival time and chart their counts as a function of the electron deflection angle, as shown in the histogram in Fig. 1(c). A distinctive coincidence peak (FWHM = 42 ns) is visible, correlating mainly coherent far-field-emitted CL photons to electrons. A background due to uncorrelated coincidences is present. We subsequently extract the energy- and coincidence-filtered electron images in Fig. 2(b). This leads to a clearly discernible signal, which differs significantly from the raw images in Fig. 2(a): the central spot, an artifact from the initial energy spread, is blanked out completely since these electrons did not produce a photon. The majority of electron counts show momenta, which are inside the red circles denoted in Fig. 2(a). This is characteristic for electrons that produce far-field transition radiation [see Figs. 1(e) and 1(f)]. On closer inspection, we see that although the sample and beam are rotationally symmetric about the beam axis, this symmetry is broken for the coincidence image. Instead, the characteristic horseshoelike shape of the photon collection mirror is revealed, as highlighted by the light red area. This is initially surprising as the CL mirror is located in the photon path and does not influence the electrons directly. At a closer look, we can understand the distribution of the electron counts using the predicted transverse momentum conservation between electron and photon for this sample, resulting in $I_\mathrm{coin}(\mathbf{p}_\perp) \propto \int dE\, \rho_\mathrm{TR}(E, \mathbf{p}_\perp)\alpha(E)\alpha_\gamma(E, -\mathbf{p}_\perp c/E)$. We defined ρ_TR as the probability density that an electron undergoes an energy loss E and acquires the transverse momentum $\mathbf{p}_\perp$ while also producing a photon which propagates to the far field in the forward direction with respect to the electron's propagation (unlike ρ, which comprises all coherent CL processes). Notably, contributions from incoherent CL are not included, but this is justified, as we consider them small compared to the coherent contributions for this sample (see Ref. [34] for more details).

Explained in terms of momentum conservation between electron and photon, if a photon is emitted to the azimuth angle ϕ, the corresponding electron is deflected in the opposite direction $\phi + \pi$. The mirror does not cover all azimuth angles [see Fig. 1(b) and [34]]; therefore, electrons are unlikely to contribute to the coincidence image unless they produce photons accepted by the mirror. The coincidence-filtered LAD images thus have to trace the shape of the photon-collection region in momentum space. Further restrictions are imposed by the fiber and detector, which only collect photons in a restricted energy range [34]. This low detection efficiency in the UV range is likely the reason for the markedly decreased coincidence signal for $E_\mathrm{c} = 4$ eV. As specifications for the optical fibers were unavailable for wavelengths below 400 nm and as their attenuation is expected to increase rapidly at such short wavelengths, we omitted the theoretical prediction for the coincidence signal in the energy range 3.5 eV to 4.5 eV. In order to account for instabilities in coincidence matching we show normalized coincidence data in Figs. 2(c) and 3(c) [34]. Theoretical predictions are in good agreement with our data (see also Fig. S3 in [34]).

Rather than applying an energy filter on the electron side, one can use a wavelength filter on the photon side. The measurements shown in Fig. 3 were performed using bandpass filters with a full width at half maximum of $2\delta_\lambda = 40$ nm at different central wavelengths λ_c. This results in a modified function $\alpha'_\gamma(\hbar\omega, \hat{\mathbf{k}}_\perp) = \alpha_\gamma(\hbar\omega, \hat{\mathbf{k}}_\perp)\mathrm{rect}[(2\pi/k_0 - \lambda_\mathrm{c})/2\delta_\lambda]$. The coincidence LAD images in Fig. 3(a) show the same horseshoelike pattern as before and scale with the photon momentum. The wavelength distribution still reflects the energy-momentum conservation between the electron-photon pairs and can be understood with the model distribution $I_\mathrm{coin}(\mathbf{p}_\perp) = \int dE\, \rho_\mathrm{TR}(E, \mathbf{p}_\perp)\alpha'_\gamma(E, -\mathbf{p}_\perp c/E)$. The theoretically predicted coincidence radial profiles [color-coded lines in Fig. 3(c)], as well as the most probable electron deflection as a function of λ_c in Fig. 3(d), show a qualitative agreement with the experimentally obtained data.

We have presented energy- and momentum-resolved coincidence measurements of electron-photon pairs, along with a theoretical description that naturally follows from the assumption of energy and momentum conservation. According to this theory, it should be possible to directly map the angular dependence of photon detection efficiency, as determined by the shape of the collecting mirror, onto the momentum distribution of the coincident electron. We are the first to demonstrate this effect—known in the photonics community as "ghost imaging" [49–51]—using electron-photon pairs, thereby also confirming the underlying phenomenon of energy-momentum conservation in coherent CL processes.

While previous momentum-resolved EELS studies showed all energy-loss mechanisms and their respective momentum transfer superimposed, combined energy and coincidence filtering allowed us to clearly separate processes which contribute to the CL signal and therefore must have resulted in the emission of a far-field photon. For electrons emitting transition radiation, we saw an overall

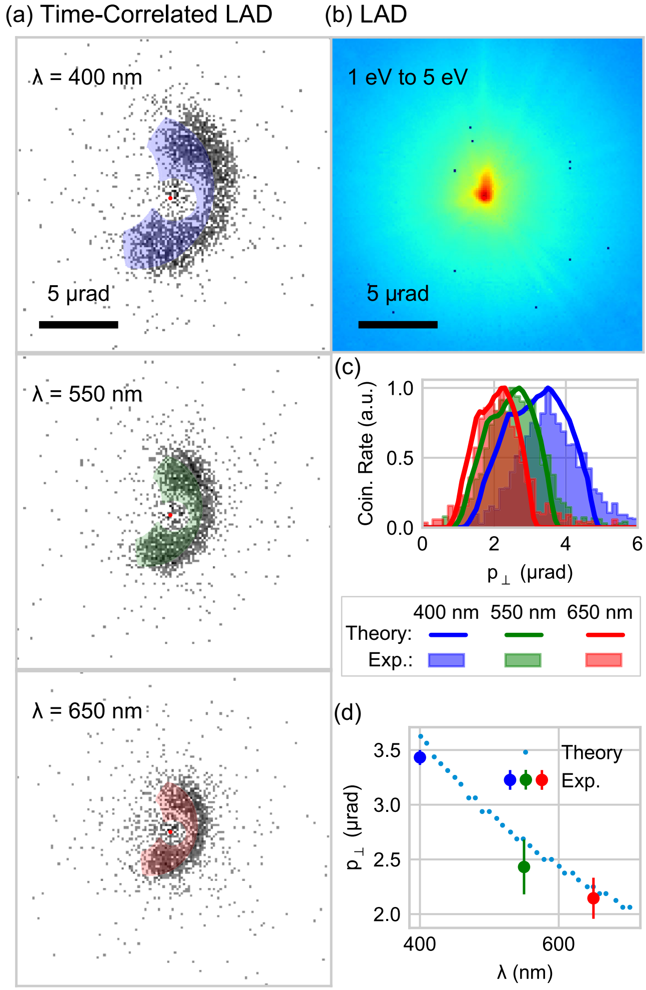

FIG. 3. Coincidence-filtered low-angle diffraction images in (a) are produced by applying different bandpass wavelength filters (FWHM = 40 nm @ 400 nm, 550 nm, 650 nm) to the photons; (b) shows the unfiltered image. The radial profiles (c) are obtained by integrating the data over the azimuthal angle ϕ. They include theoretical predictions, which agree well with the expected momentum distribution of transition radiation. In (d), the most probable deflection value for each bandpass filter is compared to the value predicted by the theoretical model. The error bars provide an estimate of the statistical uncertainty.

enhancement by a factor of ≈17 compared to the signal without coincidence filtering (i.e., energy filtering only; see Ref. [34]). This produced a clearly discernible signal which had been completely hidden in previous EELS studies. The improvement is especially pronounced in the presence of strong background signals that don't contribute to the CL. An example of this is the low-energy tail of the electron source that was strongly visible in the energy-filtered image in Fig. 2(a) but completely suppressed after coincidence filtering in Fig. 2(b).

Moreover, we argue that information about the correlated electron can be used to enhance the capabilities of CL spectroscopy. We can trace the origin of CL photons back to their production mechanism by asserting whether the momentum transfer on the electron is compatible with the characteristic dispersion relation of the photon.

We also highlight that the presented technique combines the strengths of q-EELS and CL spectroscopy when looking at radiative coherent processes. The use of optical spectroscopy generally allows for a higher energy resolution than electron energy-loss spectroscopy. As the energy loss can be measured directly on the photon instead of measuring the final energy of the electron, the resulting distribution is independent of the initial energy spread of the beam. Simultaneously, we obtain precise knowledge of the corresponding electron momentum by using the diffraction mode in the electron microscope. Future improvements on this technique, using free-space instead of fiber-coupled optics, will allow us to fully characterize the momentum correlations between the electron and the photon for any sample. Such a free-space setup may simultaneously allow for position measurements, thereby enabling us to go beyond classical correlations and probe entanglement in the joint electron-photon state. Besides its fundamental relevance for the study of CL processes, the ability to produce and characterize entangled electron-photon pairs might enable revolutionary techniques adopted from photonic quantum optics [52–54] for modern electron microscopy.

Acknowledgments—The authors thank Isobel Bicket, Michael Stöger-Pollach, Santiago Beltrán-Romero for fruitful discussions. P. H. and A. P. thank the Austrian Science Fund (FWF): Y1121, P36041, P35953. This project was supported by the ESQ-Discovery Program 2020, "A source for correlated electron-photon pairs," and the FFG-project AQUTEM. A. K. and M. H. acknowledge the support of the Czech Science Foundation GACR under the Junior Star Grant No. 23-05119M.

[1] L. Reimer and H. Kohl, *Transmission Electron Microscopy* (Springer, New York, 2008).
[2] P. E. Batson, N. Dellby, and O. L. Krivanek, Sub-Ångstrom resolution using aberration corrected electron optics, Nature (London) **418**, 617 (2002).
[3] A. Polman, M. Kociak, and F. J. García de Abajo, Electron-beam spectroscopy for nanophotonics, Nat. Mater. **18**, 1158 (2019).
[4] M. Kociak and L. F. Zagonel, Cathodoluminescence in the scanning transmission electron microscope, Ultramicroscopy **176**, 112 (2017).
[5] Z. Dang, Y. Chen, and Z. Fang, Cathodoluminescence nanoscopy: State of the art and beyond, ACS Nano **17**, 24431 (2023).
[6] E. J. R. Vesseur, R. De Waele, M. Kuttge, and A. Polman, Direct observation of plasmonic modes in Au nanowires using high-resolution cathodoluminescence spectroscopy, Nano Lett. **7**, 2843 (2007).

[7] M. Kuttge, E. J. R. Vesseur, A. F. Koenderink, H. J. Lezec, H. A. Atwater, F. J. García de Abajo, and A. Polman, Local density of states, spectrum, and far-field interference of surface plasmon polaritons probed by cathodoluminescence, Phys. Rev. B **79**, 113405 (2009).

[8] P. A. Cherenkov, Visible radiation produced by electrons moving in a medium with velocities exceeding that of light, Phys. Rev. **52**, 378 (1937).

[9] M. Stöger-Pollach, H. Franco, P. Schattschneider, S. Lazar, B. Schaffer, W. Grogger, and H. W. Zandbergen, Čerenkov losses: A limit for band gap determination and Kramers–Kronig analysis, *Micron Proceedings of the International Workshop on Enhanced Data Generated with Electrons (EDGE)* (2006), Vol. 37, pp. 396–402.

[10] M. Scheucher, T. Schachinger, T. Spielauer, M. Stöger-Pollach, and P. Haslinger, Discrimination of coherent and incoherent cathodoluminescence using temporal photon correlations, Ultramicroscopy **241**, 113594 (2022).

[11] N. Yamamoto, K. Araya, A. Toda, and H. Sugiyama, Light emission from surfaces, thin films and particles induced by high-energy electron beam, Surface Interface Anal. **31**, 79 (2001).

[12] B. J. M. Brenny, A. Polman, and F. J. García de Abajo, Femtosecond plasmon and photon wave packets excited by a high-energy electron on a metal or dielectric surface, Phys. Rev. B **94**, 155412 (2016).

[13] M. Stöger-Pollach, L. Kachtík, B. Miesenberger, and P. Retzl, Transition radiation in EELS and cathodoluminescence, Ultramicroscopy **173**, 31 (2017).

[14] J. Chen, R. Chen, F. Tay, Z. Gong, H. Hu, Y. Yang, X. Zhang, C. Wang, I. Kaminer, H. Chen, B. Zhang, and X. Lin, Low-velocity-favored transition radiation, Phys. Rev. Lett. **131**, 113002 (2023).

[15] S. J. Smith and E. M. Purcell, Visible light from localized surface charges moving across a grating, Phys. Rev. **92**, 1069 (1953).

[16] I. Kaminer, S. E. Kooi, R. Shiloh, B. Zhen, Y. Shen, J. J. López, R. Remez, S. A. Skirlo, Y. Yang, J. D. Joannopoulos, A. Arie, and M. Soljačić, Spectrally and spatially resolved Smith-Purcell radiation in plasmonic crystals with short-range disorder, Phys. Rev. X **7**, 011003 (2017).

[17] X. Bendaña, A. Polman, and F. J. García de Abajo, Single-photon generation by electron beams, Nano Lett. **11**, 5099 (2011).

[18] K. Takeuchi and N. Yamamoto, Visualization of surface plasmon polariton waves in two-dimensional plasmonic crystal by cathodoluminescence, Opt. Express **19**, 12365 (2011).

[19] T. Coenen, E. J. R. Vesseur, A. Polman, and A. F. Koenderink, Directional emission from plasmonic Yagi–Uda antennas probed by angle-resolved cathodoluminescence spectroscopy, Nano Lett. **11**, 3779 (2011).

[20] I. C. Bicket, E. P. Bellido, S. Meuret, A. Polman, and G. A. Botton, Correlative electron energy loss spectroscopy and cathodoluminescence spectroscopy on three-dimensional plasmonic split ring resonators, Microscopy **67**, i40 (2018).

[21] S. Meuret, T. Coenen, H. Zeijlemaker, M. Latzel, S. Christiansen, S. Conesa-Boj, and A. Polman, Photon bunching reveals single-electron cathodoluminescence excitation efficiency in InGaN quantum wells, Phys. Rev. B **96**, 035308 (2017).

[22] L. H. G. Tizei and M. Kociak, Spatially resolved quantum nano-optics of single photons using an electron microscope, Phys. Rev. Lett. **110**, 153604 (2013).

[23] P. Kruit, H. Shuman, and A. P. Somlyo, Detection of x-rays and electron energy loss events in time coincidence, Ultramicroscopy **13**, 205 (1984).

[24] D. Jannis, K. Müller-Caspary, A. Béché, A. Oelsner, and J. Verbeeck, Spectroscopic coincidence experiments in transmission electron microscopy, Appl. Phys. Lett. **114**, 143101 (2019).

[25] D. Jannis, K. Müller-Caspary, A. Béché, and J. Verbeeck, Coincidence detection of EELS and EDX spectral events in the electron microscope, Appl. Sci. **11**, 9058 (2021).

[26] S. Yanagimoto, N. Yamamoto, T. Yuge, H. Saito, K. Akiba, and T. Sannomiya, Time-correlated electron and photon counting microscopy, Commun. Phys. **6**, 1 (2023).

[27] A. Feist, G. Huang, G. Arend, Y. Yang, J.-W. Henke, A. S. Raja, F. J. Kappert, R. N. Wang, H. Lourenço-Martins, Z. Qiu, J. Liu, O. Kfir, T. J. Kippenberg, and C. Ropers, Cavity-mediated electron-photon pairs, Science **377**, 777 (2022).

[28] N. Varkentina, Y. Auad, S. Y. Woo, A. Zobelli, L. Bocher, J.-D. Blazit, X. Li, M. Tencé, K. Watanabe, T. Taniguchi, O. Stéphan, M. Kociak, and L. H. G. Tizei, Cathodoluminescence excitation spectroscopy: Nanoscale imaging of excitation pathways, Sci. Adv. **8**, eabq4947 (2022).

[29] A. Einstein, B. Podolsky, and N. Rosen, Can quantum-mechanical description of physical reality be considered complete?, Phys. Rev. **47**, 777 (1935).

[30] A. Konečná, F. Iyikanat, and F. J. G. de Abajo, Entangling free electrons and optical excitations, Sci. Adv. **8**, eabo7853 (2022).

[31] J.-W. Henke, H. Jeng, and C. Ropers, Quantum eraser experiments for the demonstration of entanglement between swift electrons and light, Phys. Rev. A **111**, 012610 (2025).

[32] E. Kazakevich, H. Aharon, and O. Kfir, Spatial electron-photon entanglement, Phys. Rev. Res. **6**, 043033 (2024).

[33] S. Meuret, L. H. G. Tizei, T. Cazimajou, R. Bourrellier, H. C. Chang, F. Treussart, and M. Kociak, Photon bunching in cathodoluminescence, Phys. Rev. Lett. **114**, 1 (2015).

[34] See Supplemental Material at http://link.aps.org/supplemental/10.1103/PhysRevLett.134.096901, which includes Refs. [35–38], for further detail on modeling, instrumentation, and data processing.

[35] A. A. Lucas and E. Kartheuser, Energy-loss spectrum of fast electrons in a dielectric slab. I. Nonretarded losses and Cherenkov bulk loss, Phys. Rev. B **1**, 3588 (1970).

[36] F. J. García de Abajo, Optical excitations in electron microscopy, Rev. Mod. Phys. **82**, 209 (2010).

[37] M. J. Berger, J. S. Coursey, M. A. Zucker, and J. Chang, Stopping-power and range tables for electrons, protons, and helium ions, NIST Standard Reference Database 124, National Institute of Standards and Technology (NIST), Physical Measurement Laboratory (PML) (2017).

[38] T. Poikela, J. Plosila, T. Westerlund, M. Campbell, M. D. Gaspari, X. Llopart, V. Gromov, R. Kluit, M. van Beuzekom, F. Zappon, V. Zivkovic, C. Brezina, K. Desch, Y. Fu, and A. Kruth, Timepix3: A 65K channel

hybrid pixel readout chip with simultaneous ToA/ToT and sparse readout, J. Instrum. **9**, C05013 (2014).

[39] N. Yamamoto and H. Sugiyama, Cherenkov and transition radiation generated in 200 kV electron microscope, Radiat. Eff. Defects Solids **117**, 5 (1991).

[40] N. Yamamoto and A. Toda, Imaging of Cherenkov and transition radiation from thin films and particles, Scanning Microsc. **9**, 669 (1995).

[41] N. Yamamoto, H. Sugiyama, and A. Toda, Cherenkov and transition radiation from thin plate crystals detected in the transmission electron microscope, Proc. R. Soc. A **452**, 2279 (1997).

[42] M. Stöger-Pollach, K. Bukvišová, S. Schwarz, M. Kvapil, T. Šamořil, and M. Horák, Fundamentals of cathodoluminescence in a STEM: The impact of sample geometry and electron beam energy on light emission of semiconductors, Ultramicroscopy **200**, 111 (2019).

[43] C. H. Chen, J. Silcox, and R. Vincent, Electron-energy losses in Silicon: Bulk and surface plasmons and Čerenkov radiation, Phys. Rev. B **12**, 64 (1975).

[44] H. Saito, C. Chen, and H. Kurata, Optical guided modes coupled with Čerenkov radiation excited in Si slab using angular-resolved electron energy-loss spectrum, J. Appl. Phys. **113**, 113509 (2013).

[45] R. Erni and N. D. Browning, The impact of surface and retardation losses on valence electron energy-loss spectroscopy, Ultramicroscopy **108**, 84 (2008).

[46] C. Schinke, P. Christian Peest, J. Schmidt, R. Brendel, K. Bothe, M. R. Vogt, I. Kröger, S. Winter, A. Schirmacher, S. Lim, H. T. Nguyen, and D. MacDonald, Uncertainty analysis for the coefficient of band-to-band absorption of crystalline silicon, AIP Adv. **5**, 067168 (2015).

[47] F. J. García de Abajo, A. Rivacoba, N. Zabala, and N. Yamamoto, Boundary effects in Cherenkov radiation, Phys. Rev. B **69**, 155420 (2004).

[48] E. Kröger, Berechnung der Energieverluste schneller Elektronen in dünnen Schichten mit Retardierung, Z. Phys. **216**, 115 (1968).

[49] T. B. Pittman, Y. H. Shih, D. V. Strekalov, and A. V. Sergienko, Optical imaging by means of two-photon quantum entanglement, Phys. Rev. A **52**, R3429 (1995).

[50] M. J. Padgett and R. W. Boyd, An introduction to ghost imaging: Quantum and classical, Phil. Trans. R. Soc. A **375**, 20160233 (2017).

[51] E. Rotunno, S. Gargiulo, G. M. Vanacore, C. Mechel, A. H. Tavabi, R. E. Dunin-Borkowski, F. Carbone, I. Madan, S. Frabboni, T. Guner, E. Karimi, I. Kaminer, and V. Grillo, One-dimensional “ghost imaging” in electron microscopy of inelastically scattered electrons, ACS Photonics **10**, 1708 (2023).

[52] X. Y. Zou, L. J. Wang, and L. Mandel, Induced coherence and indistinguishability in optical interference, Phys. Rev. Lett. **67**, 318 (1991).

[53] G. B. Lemos, V. Borish, G. D. Cole, S. Ramelow, R. Lapkiewicz, and A. Zeilinger, Quantum imaging with undetected photons, Nature (London) **512**, 409 (2014).

[54] M. Gilaberte Basset, F. Setzpfandt, F. Steinlechner, E. Beckert, T. Pertsch, and M. Gräfe, Perspectives for applications of quantum imaging, Laser Photonics Rev. **13**, 1900097 (2019).